Origin of superconductivity in the Weyl semimetal WTe$_2$ under pressure

Pengchao Lu,[1] Joon-Seok Kim,[2] Jing Yang,[3] Hao Gao,[1] Juefei Wu,[1] Dexi Shao,[1] Bin Li,[4] Dawei Zhou,[1,5] Jian Sun,[1,*]
Deji Akinwande,[2,6] Dingyu Xing,[1] and Jung-Fu Lin[3,6,7,†]

[1]*National Laboratory of Solid State Microstructures, School of Physics and Collaborative Innovation Center of Advanced Microstructures,*
Nanjing University, Nanjing 210093, People's Republic of China

[2]*Microelectronics Research Center, Department of Electrical and Computer Engineering,*
The University of Texas at Austin, Austin, Texas 78758, USA

[3]*Department of Geological Sciences, Jackson School of Geosciences, The University of Texas at Austin, Austin, Texas 78712, USA*

[4]*College of Science, Nanjing University of Posts and Telecommunications, Nanjing 210023, People's Republic of China*

[5]*College of Physics and Electronic Engineering, Nanyang Normal University, Nanyang 473061, People's Republic of China*

[6]*Texas Materials Institute, The University of Texas at Austin, Austin, Texas 78712, USA*

[7]*Center for High Pressure Science & Technology Advanced Research (HPSTAR), Shanghai 201203, People's Republic of China*

The structure and superconductivity of WTe$_2$ under pressure are investigated using *ab initio* calculations combined with high-pressure synchrotron x-ray diffraction and Raman spectroscopy. We find that the emergence of superconductivity in WTe$_2$ under pressure can be attributed to the phase transition from ambient T_d phase to the monoclinic $1T'$ structure phase at around 4–5 GPa, which is associated with a sliding of the WTe$_2$ layers, resulting in a critical point in the changes of Te-Te interlayer distance. This phase transition introduces an inversion center and eliminates the topological Weyl fermions in the T_d structure. Electron-phonon coupling calculations predict a similar T_c as the reported value, implying that WTe$_2$ might belong to conventional normal Bardeen-Cooper-Schrieffer superconductors.

I. INTRODUCTION

Two-dimensional (2D) transition-metal dichalcogenides (TMDs) have recently become one of the most extensively investigated materials due to their unique properties, including tunable electronic and transport properties, high mechanical flexibility, and their potential applications in vertical fabricated devices [1–5]. Among the Group VIb element TMDs, tungsten ditelluride (WTe$_2$) has recently been reported to possess a number of extraordinary physical properties. For instance, a large unsaturated magnetoresistance (MR) effect has been observed under a magnetic field of up to 60 Tesla at cryogenic temperatures below 4.5 K [6]. The enhanced MR was first described as a result of the symmetric balance between electron and hole pockets on the Fermi surface [7–11]; however, recent studies have suggested that other mechanisms can play a role in the origin of the MR [12–14]. Additionally, WTe$_2$ was recently proposed as a candidate for a new type of Weyl semimetal (WSM) (Type II) in which the Weyl points exist at the boundary of electron and hole pockets rather than at the pointlike Fermi surface in traditional WSM (Type I) systems [15–17].

Recently, pressure-induced superconductivity in WTe$_2$ was observed by two different groups [18,19], but the critical pressure for the emergence of the superconductivity varies from 2.5 GPa to 10.5 GPa in these reports. The superconducting critical temperature (Tc) reaches a maximum of around 6–7 K at certain pressure and decreases with compression to form a dome-like diagram [18,19]. Furthermore, a quantum phase transition is proposed to occur from high-pressure

electrical resistance measurements and the pressure-dependent Hall coefficient with a sign changing from the positive to the negative at around 10.5 GPa [19]. However, the relation between the structural parameters of the superconducting phase and the mechanism of the superconductivity in WTe$_2$ under pressure remains to be elucidated. A clear structural phase transition has not been thoroughly explored along with the emergence of superconductivity [18,19].

WTe$_2$ crystallizes in the orthorhombic structure with a distorted octahedral coordination (T_d) (space group $Pmn2_1$, No. 31) under ambient conditions [20], which is uniquely different from the typical trigonal prismatic structure in other TMDs, such as the $2H$-MoS$_2$, $2H$-WSe$_2$ (space group $P6_3/mmc$, No. 194) [21], or the monoclinic structure $1T'$-MoTe$_2$ (space group $P2_1/m$, No. 11) [20]. Since the crystal structure of WTe$_2$ is different from other TMDs at ambient conditions, it is reasonable to assume that the crystal structure of WTe$_2$ at high pressures may play a significant role in the origin of these aforementioned unique physical properties. However, despite its significance, high-pressure phase stability of WTe$_2$ remains largely unknown and has hindered our understanding of the fundamental physics of TMDs system in extreme environments.

In this paper, to provide new insight on the aforementioned scientific issues, we explore the structures of WTe$_2$ under pressure up to 30 GPa, with a combination of *ab initio* calculations and experiments including high-pressure synchrotron powder x-ray diffraction (XRD) and Raman measurements. We have predicted two high-pressure phases in WTe$_2$ with $P2_1/m$ and $P6_3/mmc$ symmetry, which resemble the most common $1T'$ and $2H$ structure in TMDs, respectively. Moreover, we have identified the $1T'$ phase in the high-pressure XRD and Raman experiments and resolved its structure. The T_d to $1T'$ transition

---

*Corresponding author: jiansun@nju.edu.cn
†Corresponding author: afu@jsg.utexas.edu

pressure is close to the pressure where superconductivity occurs [18,19], implying that the superconducting WTe$_2$ is actually in the 1T' phase.

II. METHODS

A. *Ab initio* calculations

We use *ab initio* random structure searching (AIRSS) [22,23] methods to find low-enthalpy structures of WTe$_2$, with system sizes up to eight formula units per simulation cell during the search. Crystal structure optimization calculations are performed by the Vienna *Ab initio* simulation package (VASP) [24], with Perdew-Burke-Ernzerhof (PBE) [25] generalized gradient approximation (GGA) exchange-correlation density functional and optB86b functional [26–28] together with van der Waals density functional (vdW-DF) corrections of Dion *et al.* [29]. The cutoff parameter for the wave functions is 400 eV, and k-point meshes are generated through Monkhorst-Pack method with a spacing of $0.02 \times 2\pi$ Å^{-1}. The phonon calculations are performed by supercell approach implemented in the PHONOPY code [30] together with VASP as the atomic force calculator, adopting a $2 \times 2 \times 2$ supercell for the 1T' and 2H structure. Electronic structure calculations are performed using the full-potential linearized augmented plane wave (FP-LAPW) method implemented in the WIEN2k [31] package. A 2000 k-point mesh for Brillouin zone (BZ) sampling and seven for the plane wave cutoff parameter $R_{MT}K_{max}$ are used in the calculation, where R is the minimum LAPW sphere radius and K_{max} is the plane wave vector cutoff. Spin-orbit coupling is taken into consideration in the second-variational calculation [32]. Transition barriers are calculated through the variable cell nudged elastic band (VC-NEB) method [33] implemented in the USPEX code [34]. The electron-phonon coupling (EPC) calculations are performed through the Quantum-ESPRESSO program [35], with a $6 \times 8 \times 4$ k-point mesh for EPC matrix and a $3 \times 4 \times 2$ q-point mesh for dynamical matrix. The cutoffs are 60 Ry for the wave functions and 600 Ry for the charge density.

B. High-pressure powder XRD and Raman experiments

A symmetric diamond anvil cell (DAC) with a pair of diamond culet size 400 μm was used for the high-pressure Raman experiments. Re gasket, initially $\sim$250 μm thick, was preindented to $\sim$40 μm and drilled at the very center to form a diameter of 200 μm for the sample chamber. A piece of WTe$_2$ sample purchased from 2D Semiconductors Company was cut into a $\sim$20 μm disk and then placed near the center of the sample chamber, along with a couple of ruby spheres used as the pressure indicator. The Ar pressure medium was loaded with the sample in the chamber using a gas loading system in the Mineral Physics Lab of The University of Texas at Austin. Raman and ruby spectra were collected using Renishaw inVia Raman spectroscopy system equipped with a 532 nm green laser and 3000 line/mm grating. In order to prevent the sample from thermal damaging, laser power was restricted to <5 mW, with integration time up to 5 minutes. Obtained spectral data were then analyzed according to background spectra, and peak position and full width at

half maximum (FWHM) extracted using Lorentzian fitting. Samples for XRD experiments were purchased from HQ Graphene, and ground using mortar to form randomly oriented powder. Externally heated DAC (EHDAC) with culet size 500 μm was used for high-pressure XRD measurements. The Titanium-Zinc-Molybdenum (TZM) gasket was preindented down to 37 μm thickness and drilled with a 180 μm hole in the center. Powder WTe$_2$ were compressed to disks and stack-loaded in the sample chamber in order to guarantee sufficient thickness and random orientation. The Au particle and ruby were also loaded as pressure indicators. Ne gas was used for pressure transmitting medium. The XRD experiments were conducted at GSECARS 13IDD beamline of the Advanced Photon Source, Argonne National Laboratory. An incident x-ray beam time of approximately 0.3344 Å in wavelength and 2–3 μm in beam size (FWHM) was used for the experiments, while XRD patterns of the sample were collected by a Mar charge-coupled device (CCD) detector. High temperature was applied either by external resistive heating or laser heating.

III. RESULTS AND DISCUSSION

The crystallographic structures of the T_d, 1T', and 2H phases are shown in Figs. 1(a) and 1(b). In the T_d phase, the tungsten atoms are sandwiched between two layers of
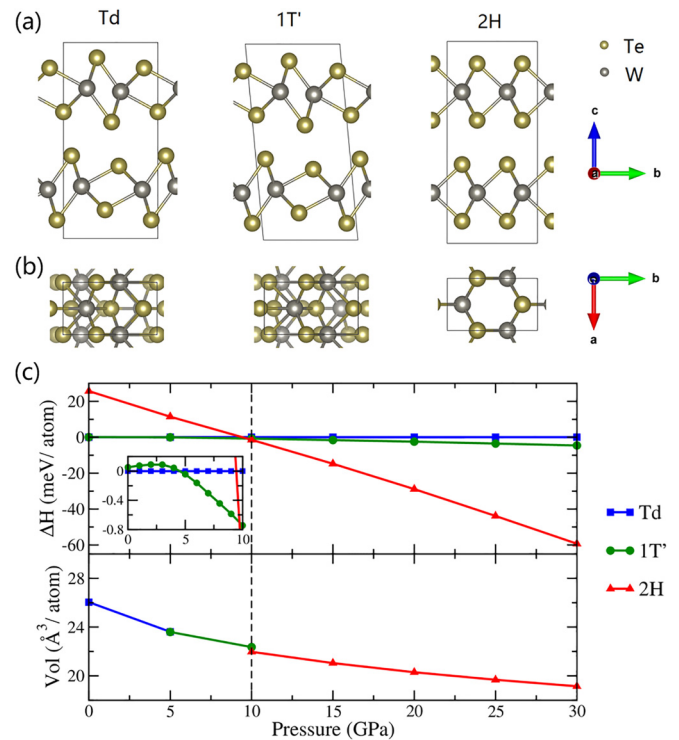

FIG. 1. (a), (b) Schematic representations of T_d, 1T', and 2H crystal structures of WTe$_2$ along the a axis and c axis, respectively. To compare 2H with T_d and 1T', the hexagonal 2H lattice is converted to orthorhombic lattice by building a $1 \times \sqrt{3}$ supercell in the xy plane. (c) Relative enthalpy difference between 2H and T_d phases as a function of pressure (top panel) and their pressure-volume curves (bottom panel). Theoretical calculations indicate two structural phase transitions, from T_d to 1T' at around 5 GPa and from the 1T' to 2H phase at about 10 GPa, respectively.

tellurium atoms in which one layer is rotated 180° with respect to the other, forming the W-Te$_6$ octahedral coordination. These layers in the T_d and $1T'$ phase exhibit buckled surface structure, whereas the high-pressure $2H$ structure only contains flat layers. The $1T'$ structure is very similar to T_d such that it can be constructed from the T_d phase with shear strain, which introduces an inversion center. Viewing the structure from the out-of-plane direction [Fig. 1(b)], tungsten and tellurium atoms are packed in a honeycomb crystal lattice for the $2H$ structure, similar to graphene or h-BN, but the structure displays a rather complicated atomic arrangement in the T_d and $1T'$ phase.

A. Theoretical calculations

The calculated enthalpy-pressure (ΔH-P) and volume-pressure (V-P) curves of WTe$_2$ are shown in Fig 1(c), which clearly show two structural phase transitions, from T_d to $1T'$ at around 5 GPa and from the $1T'$ to $2H$ phase at about 10 GPa. The T_d structure is found to be thermodynamically stable at ambient conditions, in agreement with the experimental observation [20]. However, the relative enthalpy difference between the T_d and $1T'$ phase is very small, less than 0.15 meV per atom, at ambient pressure. Moreover, calculated lattice parameters and unit cell volumes of the T_d and $1T'$ phase are very close to each other. The $2H$ phase is thermodynamically stable under high pressure, with a lower enthalpy than that of the $1T'$ phase by 59.3 meV per atom at 30 GPa. As the $2H$ structure with flat layers is more compact than the $1T'$ structure with buckled layers, there is a sudden drop in unit cell volume for the $1T'$-$2H$ transition. Compared with other typical TMDs with flat layers, WTe$_2$ at ambient conditions with uneven surface suggests that applied pressure could act to smooth the layers by providing a compressive strain and, therefore, tune the electronic properties of the TMD as well as its structure to a higher symmetry. This can be further justified by comparing with WS$_2$, which has a stable $2H$ phase at ambient condition, although WS$_2$ does not undergo any structural phase transition up to 60 GPa [36] nor an abrupt metallization at high pressures.

These octahedrally coordinated W-Te layers are held together by vdW interactions such that the dispersion correction is essential for obtaining proper interlayer spacing in theoretical calculations. As shown in the lattice parameters and volumes at 0 GPa listed in Table I, a normal GGA-PBE functional gives quite large errors on these parameters as compared to the experimental values, while the calculations based on optB86b, functional together with the vdW-DF correction that was used in this paper, gives errors less than 1.0%. Phonon dispersion calculations confirm that the $1T'$- and $2H$-WTe$_2$
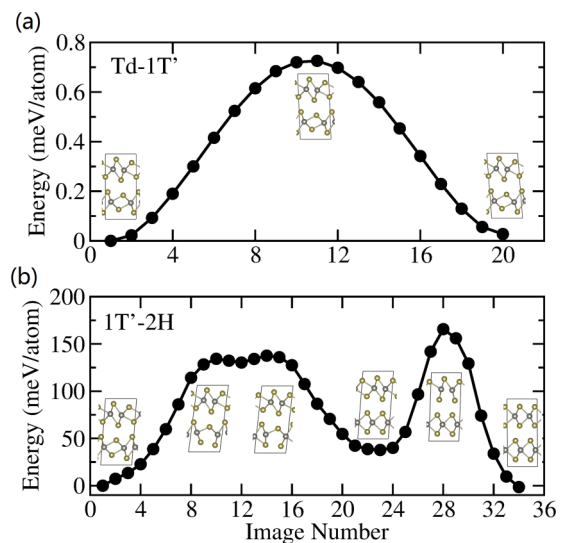

FIG. 2. Enthalpy versus pathway for (a) T_d-$1T'$ transition at 5 GPa and (b) $1T'$-$2H$ transition at 10 GPa. The T_d-$1T'$ transition path is considered as shear strain along the b axis, while the $1T'$-$2H$ transition path is considered as Te atomic layers gliding along the b axis, with four bonds broken and rebuilt per cell.

structures are dynamically stable at 0 and 15 GPa, respectively (see Appendix, Fig. 7). Moreover, the phonon spectra at 0 GPa do not exhibit modes with negative frequencies, indicating that they should be recoverable in decompression to ambient pressure if they could be synthesized experimentally. The results for $1T'$-WTe$_2$ also show that two phonon modes near the A, C, and E points undergo softening at 5 GPa.

We have also calculated the transition barriers for T_d-$1T'$ and $1T'$-$2H$ transitions using the VC-NEB method [33]. As shown in Fig. 2, due to the similarity between the T_d and $1T'$ structure, the transition path can be simply considered using an applied shear strain along the b axis. As shear strain does not break any W-Te bond, the barrier between the T_d and $1T'$ phase at 5 GPa is quite small, less than 1 meV/atom. For the $1T'$-$2H$ transition, however, no smooth transition path without breaking bond exists, as $1T'$ and $2H$ structures belong to different stacking sequences. To minimize the number of broken bonds, we have fabricated a simple transition path based on the in-plane glide. There are four Te atomic layers in the $1T'$ primitive cell, and two next-nearest ones of them are made via a glide along the b axis in opposite directions. These two glides are carried out in different stages to decrease

TABLE I. Calculated lattice parameters and volumes at 0 GPa through GGA-PBE functional and optB86b functional with vdW-DF correction, compared with the experimental values from Ref. [20]. Normal GGA-PBE functional gives quite large error, as compared to the experimental values, while the calculations based on optB86b-vdW functional gives error less than 1.0%.

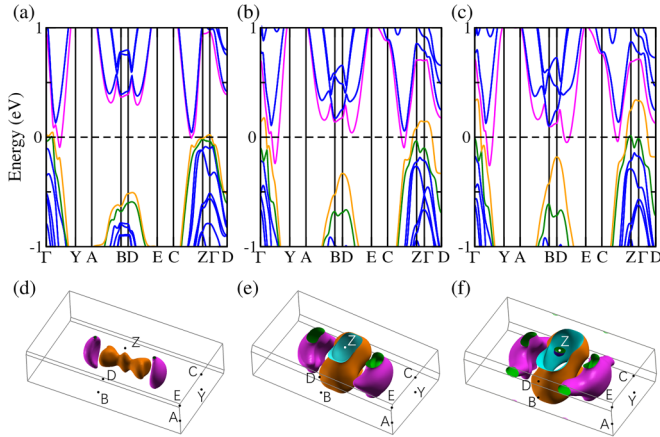|	$T_d (Pmn2_1)$			$1T' (P2_1/m)$		$2H (P6_3/mmc)$	
	PBE	optB86b	Expt.	PBE	optB86b	PBE	optB86b
a	3.500	3.499	3.496	3.500	3.499	3.558	3.533
b	6.328	6.285	6.282	6.327	6.286	3.558	3.533
c	15.803	14.211	14.070	15.612	14.217	15.167	14.110
Volume	350.00	312.52	309.00	345.48	312.42	166.26	152.56

FIG. 3. Calculated band structures and Fermi surfaces of $1T'$-WTe$_2$ with spin-orbital coupling (SOC) at 0 GPa (a), (d); 5 GPa (b), (e); and 10 GPa (c), (f). Three bands near Fermi level, two electronlike bands and one holelike band, are shown in green, orange, and magenta, respectively, while other bands are in blue. Due to the coexistence of time-reversal symmetry (TRS) and inversion symmetry, the SOC will not break spin degeneracy in $1T'$-WTe$_2$.

the energy barrier, which results in two barriers and one intermediate low-energy state. The transition barrier between the $1T'$ and $2H$ phases is estimated to be around 160 meV/atom at pressure of 10 GPa. Such a high barrier seems to be difficult to overcome in high-pressure experiments.

Analysis of the calculated band structures and Fermi surfaces, as shown in Fig. 3, suggests $1T'$-WTe$_2$ to be a semimetal as a result of the electron and hole pockets along the Γ-Y direction. There are three bands near the Fermi level, two electronlike bands and one holelike band, composing the Fermi surface. The shape of the Fermi surface is very sensitive to applied pressure, such that an increase in pressure causes an increase in the size of electron and hole pockets. This relationship indicates that $1T'$-WTe$_2$ undergoes a Lifshitz-like, or so-called electronic topological phase transition, under pressure. The band structures and the Fermi surface of the $1T'$ phase are very similar to those in the T_d phase [6], including a perfect balance between electron and hole pockets, which may cause a large unsaturated MR effect on the $1T'$-WTe$_2$ system. Lifshitz transitions, which can be seen in Fig. 3, occur when the topology of the Fermi surface develops electron and hole pockets and have been reported to coincide with the appearance of the superconductivity in iron/transition-metal based superconductor [37,38]. Application of pressure is an efficient method to tune the lattice constants and thereby atomic interactions, which has been reported to produce new topological phases of materials [39]. This naturally draws the question whether pressure could change the topological properties of WTe$_2$. However, in the T_d phase, spin degeneracy is broken by the spin-orbit coupling due to the absence of an inversion symmetry, while the spin degeneracy will remain in the $1T'$ phase, which contains an inversion center. Thus, the Weyl fermions in the ambient T_d phase should disappear after the structure phase transition. In previous works [18,19], it was proposed that superconductivity found in WTe$_2$ emerges from a suppressed large MR (LMR) state under high pressure.
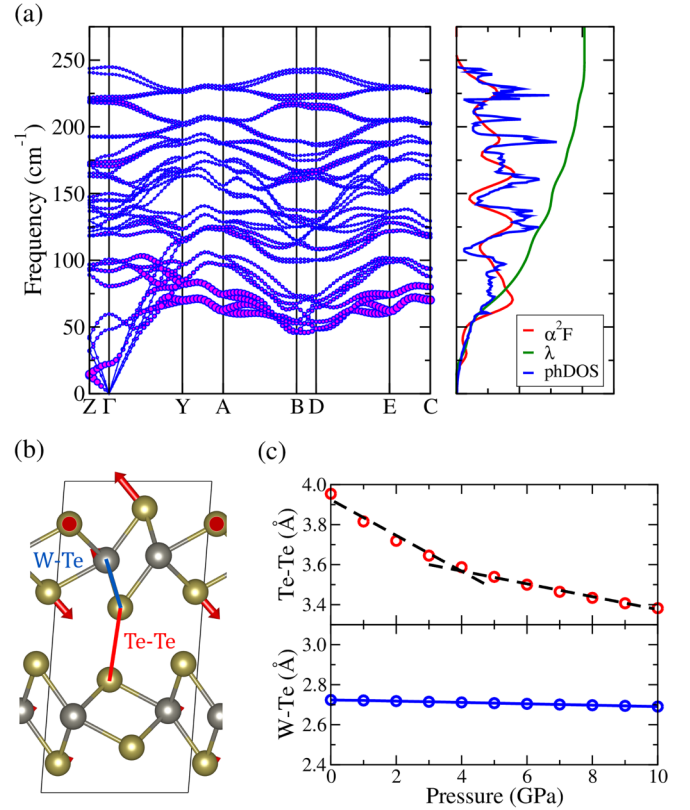

FIG. 4. (a) Theoretical phonon dispersions of $1T'$-WTe$_2$ at 10 GPa. The size of the dots represents density of electron-phonon spectral function $\alpha^2F(\omega)$. Phonon density of state (DOS) and the electron-phonon integral $\lambda(\omega)$ are also shown on the right panel. (b) Schematic representations of $1T''$-WTe$_2$ crystal structures along the a axis. Red arrows represent one TA vibrational mode (B_u symmetry) near A point. (c) Theoretical Te-Te bond length (top panel) and W-Te bond length (bottom panel) of $1T'$-WTe$_2$ as a function of pressure. The Te-Te bond length shows a rapid decrease with increasing pressure until around 4 GPa and a slow decrease with further increase in pressure. The dashed lines fit for two phases, i.e., the normal $1T'$ phase and the collapsed $1T'$, in two pressure regions.

The critical pressure of superconductivity around 2.5 GPa is close to the T_d-$1T'$ transition pressure from this paper; it is conceivable that superconductivity in WTe$_2$ emerges from the $1T'$ phase rather than the T_d phase.

In order to further understand the superconductivity mechanism in the system, we have performed *ab initio* calculations for the EPC of $1T'$-WTe$_2$ using the density functional perturbation theory [40]. The superconducting transition temperature can be estimated by the Allen and Dynes modified McMillan formula [41]: $T_c = \frac{\langle\omega\rangle}{1.20}\exp(-\frac{1.04(1+\lambda)}{\lambda-\mu^*(1+0.62\lambda)})$, where the parameter λ is a dimensionless measure of the Eliashberg electron-phonon spectral function $\alpha^2F(\omega)$, expressed as $\lambda = 2\int_0^\infty d\omega\ \alpha^2F(\omega)/\omega$. Using a common value of $\mu^* = 0.1$, the T_c in $1T'$-WTe$_2$ at 10 GPa is estimated to be $2 \sim 4$ K with a different broadening factor, which agrees well with the measurements [18,19]. Theoretical phonon dispersions of $1T'$-WTe$_2$ at 10 GPa are shown in Fig. 4(a). It seems that the low frequency phonon modes indeed have significant contributions
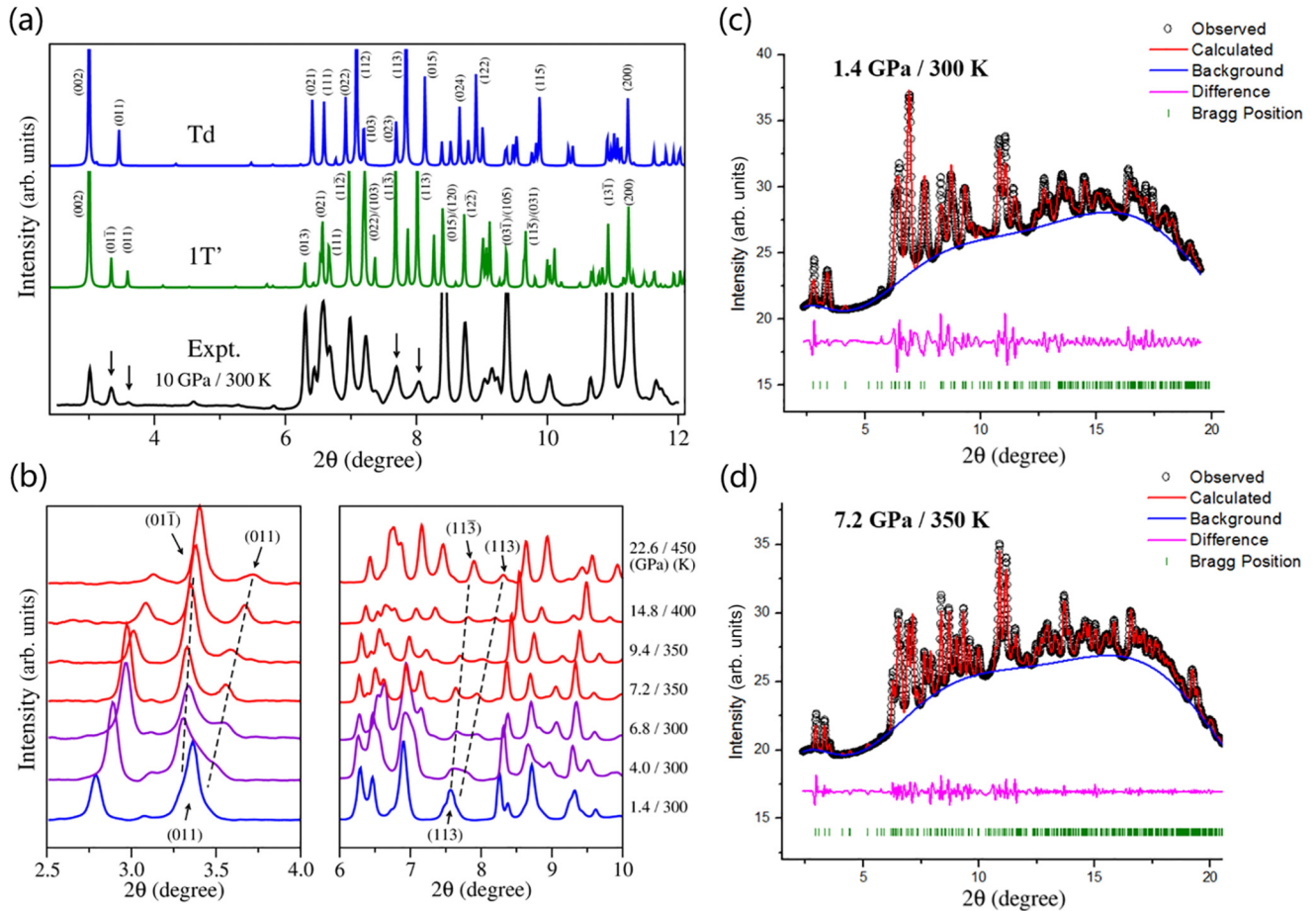
FIG. 5. (a) Simulated XRD patterns of the optimized structures at 10 GPa, compared with experimental values at 10 GPa/300 K. The wavelength is 0.3344 Å. Black arrows in the experimental spectrum indicates the split (011) and (113) peaks. (b) Experimental XRD spectra under high pressure. (011) and (113) peaks clearly show splitting, which is evidence of the phase transition from T_d to $1T'$ as pressure/temperature increases. High-pressure x-ray powder diffraction spectra for (c) T_d phase 1.4 GPa/300 K and (d) $1T'$ phase 7.2 GPa/350 K. The two experimental data matched well with calculated Bragg peaks. The Le Bail method was used in order to fit the diffraction, where the layered WTe_2 has preferred orientations and therefore highly textured structure.

to the EPC coupling. One transverse acoustic (TA) vibrational mode (B_u mode) near A point, as shown in Fig. 4(b), is mainly contributed from Te-Te interlayer vibrations. Figure 4(c) shows the calculated interlayer Te-Te distance and W-Te bond length within the layer of $1T'$-WTe_2 as a function of pressure up to 10 GPa. The Te-Te distance exhibits an obvious variation under pressure, while the intralayer W-Te bond length is almost unchanged. This implies that the effect of compression is mostly on interlayers because of the unique anisotropy of the vdW structure. The slope of the variation of the Te-Te distance exhibits two linear regions: a rapid decrease with increasing pressure until around 4 GPa and a slow decrease with further increase in pressure, which suggests an irregular point with compression. This corresponds to the T_d-to-$1T'$ phase transition, where pressure-induced shear strain readjusts Te atoms and introduces an inversion symmetry. Together with the observation of the pressure-induced superconductivity in $ZrTe_5$ [42] and $MoTe_2$ [43], the softening of the interlayer Te-Te vibration modes, resulting from compression of zig-zag TMD layers, can be reasonably correlated with the emergence of the superconductivity in TMDs.

B. High-pressure experiments

To check our theoretical predictions, we performed high-pressure synchrotron XRD and Raman experiments. Analysis of the high pressure XRD spectra has confirmed the theoretically predicted T_d-$1T'$ transition. In the simulated XRD patterns in Fig. 5(a), the $1T'$ phase can be effectively distinguished from the T_d phase by the splitting of (011) and (113) peaks. Evolution of the experimental patterns as pressure increases in Fig. 5(b) clearly shows such splitting, despite somewhat broad peaks due to the existence of deviatoric stress under high pressures. The diffraction signal of the $1T'$ phase first appears at around 4 GPa, which agrees very well with the theoretical prediction [Fig. 5(b), violet lines]. After applying external heating to ∼350 K at high pressures, the $1T'$ diffraction signal is significantly enhanced and becomes dominant at higher pressure/temperature [Fig. 5(b), red lines]. A representative experimental XRD spectrum of WTe_2 is compared with theoretical prediction of the $1T'$ and T_d phase, which resembles the $1T'$ phase in overall range of the spectra [Fig. 5(a)]. The T_d and $1T'$ structure can be fitted to the XRD patterns measured at 1.4 and 7.6 GPa, respectively, as shown
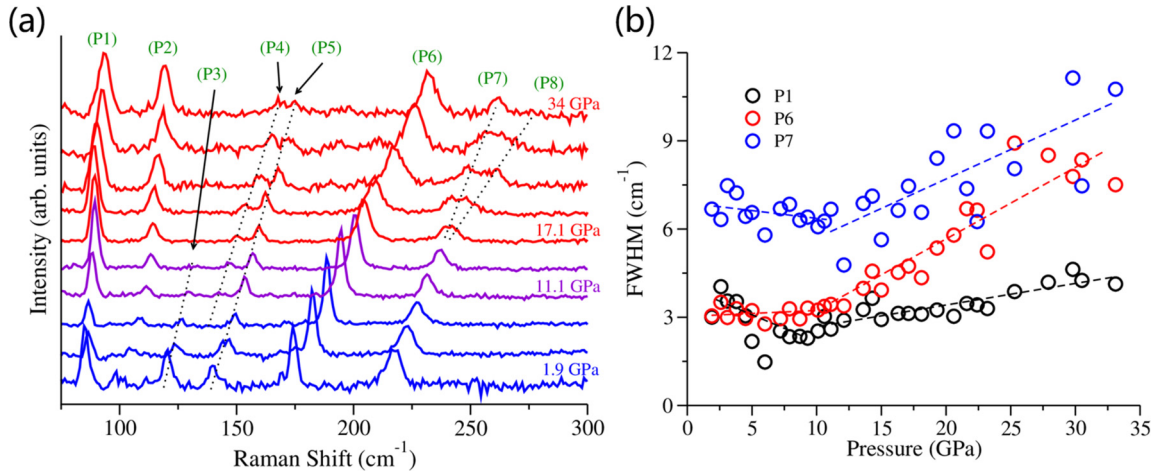
FIG. 6. (a) Experimental Raman spectra of WTe$_2$ under pressure. Dashed lines are guided line of the peaks, showing discontinuity of *P3* and *P4* and phonon splitting of *P8* from *P7*. (b) The FWHM of *P1*, *P6*, and *P7*, indicating dramatic broadening of *P6* and *P7* at pressure >11 GPa. This implies possible rising of Raman modes in the 1*T'* phase, as predicted from theoretical calculation. Dashed lines are linear fit lines for the range before and after 11 GPa.

in Figs. 5(c) and 5(d). The Le Bail method was used to fit the experimental XRD data because WTe$_2$ is intrinsically layered and therefore can develop textures at high pressures, which hinders Rietveld refinement to provide suitable analysis. We note that the 1*T'*-to-2*H* phase transition was not observed in the high-pressure experiment, even with increased temperature up to 22.9 GPa and 450 K for EHDAC and 15.4 GPa and >2000 K for laser heated DAC (LHDAC), respectively. This is consistent with our calculations on transition barriers, where the transition barrier from 1*T'* to 2*H* is significantly high. The transition may be a sluggish process due to the high kinetic barriers; therefore, the equilibration time during the experiment was not long enough to fully transform to 2*H* phase, even if the applied pressure and temperature were sufficiently high. As forming alloyed MoTe$_2$-WTe$_2$ monolayers can decrease critical temperatures of *T'*-*H* transition efficiently [44], introducing Mo-doping may scale down the transition pressure of 1*T'*-2*H* transition in bulk WTe$_2$. Because the focus of the present paper is to relate superconductivity to the structural phase of WTe$_2$ at relatively low pressures, the 2*H* phase is estimated to be semiconducting below 18 GPa (see Appendix, Fig. 8), thus no additional experiments were designed to apply higher pressure and temperature.

High-pressure Raman measurements also suggest the occurrence of a structural phase transition at around 11 GPa. There are 33 irreducible representations of the optical phonons in T_d-WTe$_2$ at the Γ point for the $C_{2v}(mm2)$ group: $\Gamma_{\text{optic}} = 11A_1 + 6A_2 + 5B_1 + 11B_2$, which are all Raman active. Seven of them are observed in laser spectroscopic experiments for the T_d structure under ambient pressure [45,46], including $A_1(78.9 \, \text{cm}^{-1})$, $A_2(88.4 \, \text{cm}^{-1})$, $A_2(109.9 \, \text{cm}^{-1})$, $A_1(114.6 \, \text{cm}^{-1})$, $A_1(129.9 \, \text{cm}^{-1})$, $A_1(160.6 \, \text{cm}^{-1})$, and $A_1(207.7 \, \text{cm}^{-1})$ [45]. For the 1*T'* structure with the point group $C_{2h}(2/m)$, there are 33 optic modes at the Γ point as well: $\Gamma_{\text{optic}} = 12A_g + 5A_u + 6B_g + 10B_u$. Eighteen of them, $12A_g + 6B_g$, are Raman active modes. The evolution of these modes under high pressure is shown in Fig. 6. Six Raman peaks measured in ambient pressure, denoted as *P1*, *P2*, *P3*, *P5*, *P6*,

and *P7*, undergo blueshift as pressure increases, and the overall trend shows a good match with calculated results up to 30 GPa. The discontinuity of Raman bands above 11 GPa, such as the vanishing *P3* band and the occurrence of the *P4* band with a higher frequency, suggests that T_d-1*T'* transition has occurred [see Fig. 6(a)]. As shown in Fig. 6(b), the pressure dependence of the FWHM of the Raman bands *P6* and *P7* rapidly increased from $-0.02 \, \text{cm}^{-1}/\text{GPa}$ to $0.25 \, \text{cm}^{-1}/\text{GPa}$ and from $-0.05 \, \text{cm}^{-1}/\text{GPa}$ to $0.19 \, \text{cm}^{-1}/\text{GPa}$, respectively, at ~ 11 GPa. When compared to the relatively slow broadening of the *P1* ($-0.1 \, \text{cm}^{-1}/\text{GPa}$ to $0.07 \, \text{cm}^{-1}/\text{GPa}$) and *P2* band, which both remain sharp at high pressure [Fig. 6(a)], broadening of *P6* and *P7* may be attributed to the appearance of the 1*T'* phase.

IV. CONCLUSION

In summary, the combination of the crystal structural prediction and first-principles calculations in this paper allows us to predict that WTe$_2$ undergoes two structural phase transitions: $T_d(Pmn2_1)$ to $1T'(P2_1/m)$ transition at around 4–5 GPa and $1T'(P2_1/m)$ to $2H(P6_3/mmc)$ phase at around 10 GPa. High-pressure XRD and Raman measurements confirm the T_d-1*T'* transition and give consistent critical transition pressure at around 4–5 GPa. Since the transition pressure is very close to the emergence pressure of the superconductivity and the irregular points in the Te-Te distance variations and modes softening in the phonon spectra occur across the transition, we thus attribute the pressure-induced superconductivity in WTe$_2$ to the T_d-1*T'* structure transition. Based on the analysis of the transition path and energy barriers, we found that the barrier for the T_d-1*T'* transition is very low, and the one for the 1*T'*-2*H* transition is very high. The latter is likely the reason why the 2*H* phase has not been observed experimentally. These results show that applied pressure not only influences the stacking sequences but also the electronic structures of the layered TMD materials, giving rise to very rich electronic features of WTe$_2$ at high pressures and low temperatures.
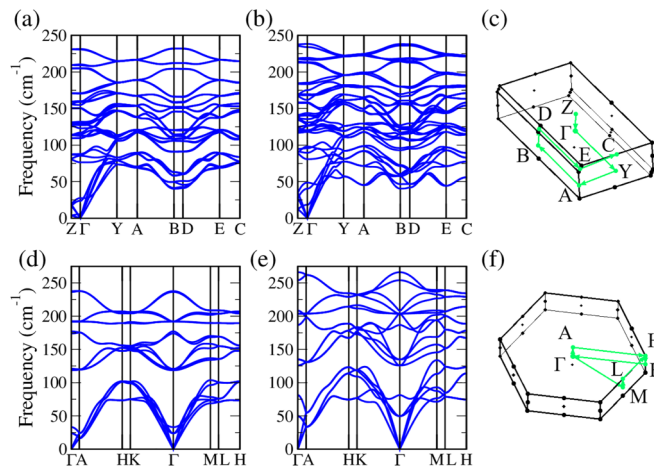
APPENDIX

FIG. 7. Phonon dispersion relations of $1T'$-WTe$_2$ (a) 0 GPa and (b) 5 GPa and $2H$-WTe$_2$ at (d) 0 GPa and (e) 15 GPa, with their first Brillouin zones (c) and (f), respectively. These two structures are confirmed to be dynamically stable as the phonon dispersions exhibit no negative-frequency modes. Moreover, it should be recoverable in decompression to ambient pressure if they could be synthesized experimentally. Two phonon modes near the A, C, and E points goes soft in $1T'$-WTe$_2$ at 5 GPa.
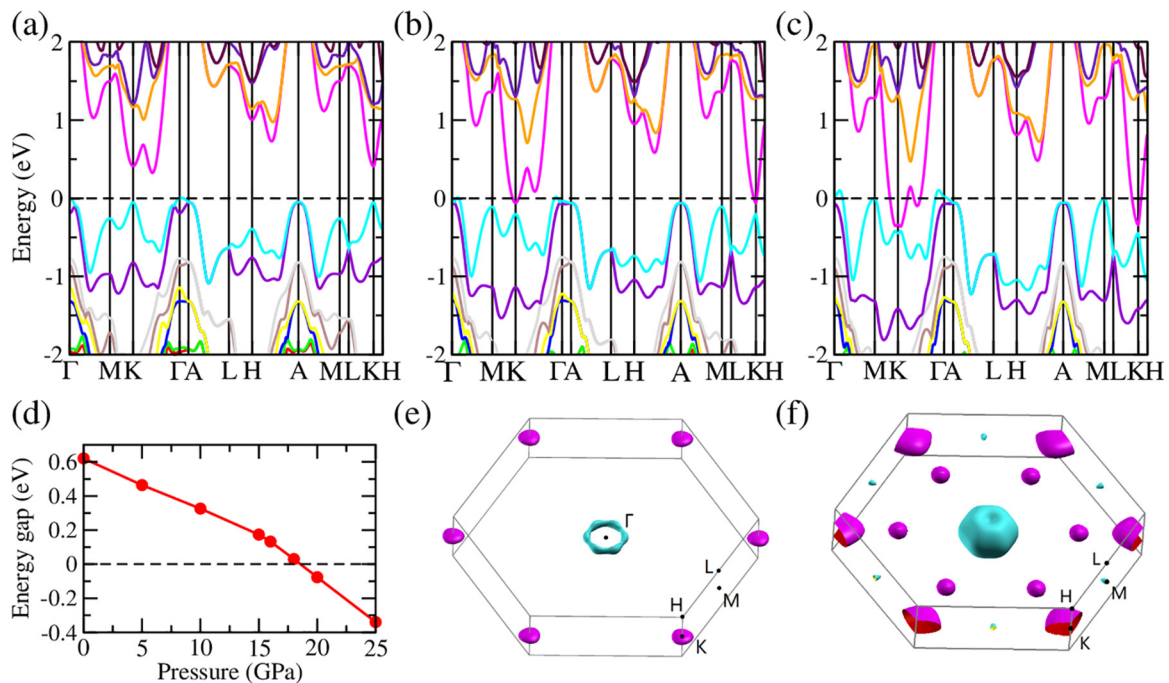

FIG. 8. Calculated band structures of $2H$-WTe$_2$ with SOC at 10 GPa (a), 20 GPa (b), 30 GPa (c), energy gap as a function of pressure (d), and Fermi surface at 20 GPa (e) and 30 GPa (f).

[1] K. F. Mak, C. Lee, J. Hone, J. Shan, and T. F. Heinz, Phys. Rev. Lett. **105**, 136805 (2010).

[2] C. Lee, H. Yan, L. E. Brus, T. F. Heinz, J. Hone, and S. Ryu, ACS Nano **4**, 2695 (2010).

[3] A. P. Nayak, T. Pandey, D. Voiry, J. Liu, S. T. Moran, A. Sharma, C. Tan, C.-H. Chen, L.-J. Li, M. Chhowalla, J.-F. Lin, A. K. Singh, and D. Akinwande, Nano Lett. **15**, 346 (2015).

[4] A. P. Nayak, S. Bhattacharyya, J. Zhu, J. Liu, X. Wu, T. Pandey, C. Jin, A. K. Singh, D. Akinwande, and J.-F. Lin, Nat. Commun. **5**, 3731 (2014).

[5] A. K. Geim and I. V. Grigorieva, Nature **499**, 419 (2013).

[6] M. N. Ali, J. Xiong, S. Flynn, J. Tao, Q. D. Gibson, L. M. Schoop, T. Liang, N. Haldolaarachchige, M. Hirschberger, N. P. Ong, and R. J. Cava, Nature **514**, 205 (2014).

[7] H. Y. Lv, W. J. Lu, D. F. Shao, Y. Liu, S. G. Tan and Y. P. Sun, Europhys. Lett. **110**, 37004 (2015).

[8] Z. Zhu, X. Lin, J. Liu, B. Fauqué, Q. Tao, C. Yang, Y. Shi, and K. Behnia, Phys. Rev. Lett. **114**, 176601 (2015).

[9] I. Pletikosić, M. N. Ali, A. V. Fedorov, R. J. Cava, and T. Valla, Phys. Rev. Lett. **113**, 216601 (2014).

[10] F. Xiang, M. Veldhorst, S. Dou, and X. Wang, Europhys. Lett. **112**, 37009 (2015).

[11] P. L. Cai, J. Hu, L. P. He, J. Pan, X. C. Hong, Z. Zhang, J. Zhang, J. Wei, Z. Q. Mao, and S. Y. Li, Phys. Rev. Lett. **115**, 057202 (2015).

[12] M. M. Parish and P. B. Littlewood, Nature **426**, 162 (2003).

[13] J. Jiang, F. Tang, X. C. Pan, H. M. Liu, X. H. Niu, Y. X. Wang, D. F. Xu, H. F. Yang, B. P. Xie, F. Q. Song, P. Dudin, T. K. Kim, M. Hoesch, P. K. Das, I. Vobornik, X. G. Wan, and D. L. Feng, Phys. Rev. Lett. **115**, 166601 (2015).

[14] Y. Wang, K. Wang, J. Reutt-Robey, J. Paglione, and M. S. Fuhrer, Phys. Rev. B **93**, 121108(R) (2016).

[15] A. A. Soluyanov, D. Gresch, Z. Wang, Q.-S. Wu, M. Troyer, X. Dai, and B. Andrei Bernevig, Nature **527**, 495 (2015).

[16] F. Y. Bruno, A. Tamai, Q. S. Wu, I. Cucchi, C. Barreteau, A. de la Torre, S. McKeown Walker, S. Riccò, Z. Wang, T. K. Kim, M. Hoesch, M. Shi, N. C. Plumb, E. Giannini, A. A. Soluyanov, and F. Baumberger, Phys. Rev. B **94**, 121112(R)(2016).

[17] C. Wang, Y. Zhang, J. Huang, S. Nie, G. Liu, A. Liang, Y. Zhang, B. Shen, J. Liu, C. Hu, Y. Ding, D. Liu, Y. Hu, S. He, L. Zhao, L. Yu, J. Hu, J. Wei, Z. Mao, Y. Shi *et al.*, arXiv:1604.04218 (2016).

[18] X.-C. Pan, X. Chen, H. Liu, Y. Feng, Z. Wei, Y. Zhou, Z. Chi, L. Pi, F. Yen, F. Song, X. Wan, Z. Yang, B. Wang, G. Wang, and Y. Zhang, Nat. Commun. **6**, 7805 (2015).

[19] D. Kang, Y. Zhou, W. Yi, C. Yang, J. Guo, Y. Shi, S. Zhang, Z. Wang, C. Zhang, S. Jiang, A. Li, K. Yang, Q. Wu, G. Zhang, L. Sun, and Z. Zhao, Nat. Commun. **6**, 7804 (2015).

[20] B. E. Brown, Acta Cryst. **20**, 268 (1966).

[21] M. Chhowalla, H. Suk Shin, G. Eda, L.-J. Li, K. Ping Loh, and H. Zhang, Nature Chemistry **5**, 263 (2013).

[22] C. J. Pickard and R. J. Needs, Phys. Rev. Lett. **97**, 045504 (2006).

[23] C. J. Pickard and R. J. Needs, J. Phys. Condens. Mat. **23**, 053201 (2011).

[24] G. Kresse and J. Furthmüller, Comput. Mater. Sci. **6**, 15 (1996).

[25] J. P. Perdew, K. Burke, and M. Ernzerhof, Phys. Rev. Lett. **77**, 3865 (1996).

[26] G. Román-Pérez and J. M. Soler, Phys. Rev. Lett. **103**, 096102 (2009).

[27] J. Klimeš, D. R. Bowler, and A. Michaelides, Phys. Rev. B **83**, 195131 (2011).

[28] T. Thonhauser, V. R. Cooper, S. Li, A. Puzder, P. Hyldgaard, and D. C. Langreth, Phys. Rev. B **76**, 125112 (2007).

[29] M. Dion, H. Rydberg, E. Schröder, D. C. Langreth, and B. I. Lundqvist, Phys. Rev. Lett. **92**, 246401 (2004).

[30] A. Togo, F. Oba, and I. Tanaka, Phys. Rev. B **78**, 134106 (2008).

[31] P. Blaha, K. Schwarz, G. Madsen, D. Kvasnicka, and J. Luitz, *WIEN2k: An Augmented Plane Wave plus Local Orbitals Program for Calculating Crystal Properties* (Karlheinz Schwarz, Technische Universität Wien, Vienna, 2001).

[32] J. Kuneš, P. Novák, R. Schmid, P. Blaha, and K. Schwarz, Phys. Rev. B **64**, 153102 (2001).

[33] G. R. Qian, X. Dong, X.-F. Zhou, Y. Tian, A. R. Oganov, and H.-T. Wang, Comput. Phys. Commun. **184**, 2111 (2013).

[34] A. R. Oganov and C. W. Glass, J. Chem. Phys. **124**, 244704 (2006).

[35] P. Giannozzi, S. Baroni, N. Bonini, M. Calandra, R. Car, C. Cavazzoni, D. Ceresoli, G. L. Chiarotti, M. Cococcioni, I. Dabo, A. Dal Corso, S. de Gironcoli, S. Fabris, G. Fratesi, R. Gebauer, U. Gerstmann, C. Gougoussis, A. Kokalj, M. Lazzeri, L. Martin-Samos *et al.*, J. Phys. Condens. Mat. **21**, 395502 (2009).

[36] A. P. Nayak, Z. Yuan, B. Cao, J. Liu, J. Wu, S. T. Moran, T. Li, D. Akinwande, C. Jin, and J.-F. Lin, ACS Nano, **9**, 9117 (2015).

[37] C. Liu, T. Kondo, R. M. Fernandes, A. D. Palczewski, E. D. Mun, N. Ni, A. N. Thaler, A. Bostwick, E. Rotenberg, J. Schmalian, S. L. Bud'ko, P. C. Canfield, and A. Kaminski, Nat. Phys. **6**, 419 (2010).

[38] Y. Wu, N. H. Jo, M. Ochi, L. Huang, D. Mou, S. L. Bud'ko, P. C. Canfield, N. Trivedi, R. Arita, and A. Kaminski, Phys. Rev. Lett. **115**, 166602 (2015).

[39] Y. Zhou, P. Lu, Y. Du, X. Zhu, G. Zhang, R. Zhang, D. Shao, X. Chen, X. Wang, M. Tian, J. Sun, X. Wan, Z. Yang, W. Yang, Y. Zhang, and D. Xing, Phys. Rev. Lett. **117**, 146402 (2016).

[40] S. Baroni, S. de Gironcoli, A. D. Corso, and P. Giannozzi, Rev. Mod. Phys. **73**, 515 (2001).

[41] P. B. Allen and R. C. Dynes, Phys. Rev. B **12**, 905 (1975).

[42] Y. Zhou, J. Wu, W. Ning, N. Li, Y. Du, X. Chen, R. Zhang, Z. Chi, X. Wang, X. Zhu, P.o Lu, C. Ji, X. Wan, Z. Yang, J. Sun, W. Yang, M. Tian, Y. Zhang, and H.-k. Mao, Proc. Nat. Acad. Sci. USA, **113**, 2904 (2016).

[43] Y. Qi, P. G. Naumov, M. N. Ali, C. R. Rajamathi, W. Schnelle, O. Barkalov, M. Hanfland, S.-C. Wu, C. Shekhar, Y. Sun, V. Süß, M. Schmidt, U. Schwarz, E. Pippel, P. Werner, R. Hillebrand, T. Förster, E. Kampert, S. Parkin, R. J. Cava, C. Felser, B. Yan, and S. A. Medvedev, Nat. Commun. **7**, 11038 (2016).

[44] K.-A. N. Duerloo and E. J. Reed, ACS Nano **10**, 289 (2016).

[45] W.-D. Kong, S.-F. Wu, P. Richard, C.-S. Lian, J.-T. Wang, C.-L. Yang, Y.-G. Shi, and H. Ding, Appl. Phys. Lett. **106**, 081906 (2015).

[46] C.-H. Lee, E. Cruz-Silva, L. Calderin, M. A. T. Nguyen, M. J. Hollander, B. Bersch, T. E. Mallouk, and J. A. Robinson, Sci. Rep. **5**, 10013 (2015).